Chapter 12   Quantitative In Vivo Imaging of Tissue Absorption, Scattering, and Hemoglobin Concentration in Rat Cortex Using Spatially Modulated Structured Light

David J. Cuccia, David Abookasis, Ron D. Frostig, and Bruce J. Tromberg.

12.1. INTRODUCTION

Significant changes in blood flow or in the integrity of cerebral vessels are believed to cause cerebrovascular disease (CVD) and to contribute to dementias including Alzheimer's disease [1]. Stroke, the most serious form of CVD, is one of the leading causes of death and adult disability worldwide. Acute treatments for stroke, however, are severely limited. Neuroprotective drugs under development show promise at halting the ischemic cascade, but as yet, no such compound has received federal approval in the United States. One of the biggest limitations to this development is the lack of understanding of the mechanisms by which cerebral vessels react to factors such as ischemia, inflammation, blood pressure changes, metabolic demands, and trauma [2]. In order to address these fundamental questions, functional brain imaging techniques such as fMRI and intrinsic signal optical imaging (ISOI) have emerged as tools to visualize and quantify cerebral hemodynamics.

In the neuroscience community, ISOI has long been used to study the organization and functional architecture of different cortical regions in animals and humans [3–5] (see other chapters in this book). Three sources of ISOI signals that affect the intensity of diffusely reflected light derive from characteristic physiologic changes in the cortex. For functional neuronal activation, these have been observed to occur over a range of timescales, including (1) light scattering changes, both fast (over 10 s of milliseconds) and slow (i.e., > ~0.5 s) (2) early (~0.5–2.5 s) absorption changes from alterations in chromophore redox status, i.e., the oxy/deoxy-hemoglobin ratio (known as the "initial dip" period), and (3), slower (~2–10 s) absorption changes due to blood volume increase (correlated with the fMRI BOLD signal). Light scattering changes have been attributed to interstitial volume changes resulting from cellular swelling, organelle swelling due to ion and water movement, capillary expansion, and neurotransmitter release [6,7]. The slower absorption factors have been demonstrated to correlate with the changes in metabolic demand and subsequent hemodynamic cascades following neuronal activation [4,8,9].

Using animal models of acute and chronic brain injury, ISOI has been used to quantify the acute hemodynamic events in response to stroke, including focal ischemia and cortical spreading depression (CSD) [10–21]. Researchers have also used ISOI to locate and quantify the spatial extent of the stroke injury, including ischemic core, penumbra, and healthy tissue zones [18,22]. CSD also plays a key role in migraine headache, and recent laser speckle imaging studies have revealed the neurovascular coupling mechanism to the transmission of headache pain [23,24].

To fully understand the underlying mechanisms in vascular changes associated with cerebrovascular diseases such as stroke, an optical imaging technique that has the capability to rapidly separate absorption from scattering effects can enhance the information content of traditional ISOI, enabling (1) more accurate quantitation of hemodynamic function, (2) isolation of the electro-chemical changes characterized by light scattering, and (3) longitudinal chronic injury studies of function where structural reorganization due to neovascularization can cause significant alterations in scattering [25,26].

Quantitative diffuse optical methods [27] such as spatially-resolved reflectance, diffuse optical spectroscopy (DOS), and tomography (DOT), and diffuse correlation spectroscopy (DCS) possess exquisite sensitivity to these functional and structural alterations associated with brain injury, and have been applied to the study of CSD [11,15,28]. DOS and DOT utilize the near-infrared spectral region (600–1000 nm) to separate and quantify the multispectral absorption (μ_a) and reduced scattering coefficients (μ_s'), providing quantitative determination of several important biological chromophores such as deoxy-hemoglobin (HbR), oxy-hemoglobin (HbO$_2$), water (H$_2$O), and lipids. Concentrations of these

chromophores represent the direct metrics of tissue function such as blood volume fraction, tissue oxygenation, and edema. Additionally, the scattering coefficient contains important structural information about the size and density of scatterers and can be used to assess tissue composition (exctracellular matrix proteins, cell nuclei, mitochondria) as well as follow the process of tissue remodeling (wound healing, cancer progression). DOS utilizes a limited number of source-detector positions, e.g., 1–2, but often employs broadband content in temporal and spectral domains [29]. In contrast, DOT typically utilizes a limited number of optical wavelengths (e.g., 2–6) and a narrow temporal bandwidth, but forms higher resolution images of subsurface structures by sampling a large number of source-detector "views." To achieve maximal spatial resolution, the ideal DOT design would employ thousands of source-detector pairs and wavelengths. However, several engineering considerations including measurement time and instrument complexity currently limit the practicality of this approach.

In this chapter we present the basic principles of a new, noncontact quantitative optical imaging technology, modulated imaging (MI) [30–32], and provide examples of MI performance in 2 rat models of brain injury, cortical spreading depression (CSD) and stroke. MI enables both DOS and DOT concepts with high spatial (<1 mm) and temporal resolution (<1 s) in a simple, scan-free platform. MI is capable of both separating and spatially-resolving optical absorption and scattering parameters, allowing wide-field quantitative mapping of tissue optical properties. While compatible with time-modulation methods, MI alternatively uses spatially modulated illumination for imaging of tissue constituents. Periodic illumination patterns of various spatial frequencies are projected over a large area of a sample. The diffusely reflected image is modified from the illumination pattern due to the turbidity of the sample. Typically, sine-wave illumination patterns are used. The demodulation of these spatially modulated waves characterizes the modulation transfer function (MTF) of the material, and embodies the sample optical property information.

12.2. METHODS AND INSTRUMENTATION

12.2.1. Modulated Imaging Spectroscopy

The MI instrument platform was introduced originally by Cuccia et al. [30] Based on this design, we have developed a custom multispectral near-infrared (NIR) MI spectroscopy system capable of imaging between 650 and 1000 nm. A diagram of this system is shown in Figure 12.1.

Broadband NIR illumination is provided by an intensity-stabilized 250 W quartz-tungsten-halogen (QTH) lamp (Oriel QTH Source with Light Intensity Controller, Newport Corporation-Oriel Instruments, Stratford, Connecticut). Light is collimated and refocused with a pair of aspheric F/#0.7 optical lens systems (Oriel Aspherab). A custom-sized 3.5 in square hybrid hot mirror (Reynard Corporation, i.e., R00670-00) was placed between the lenses to limit the illumination to wavelengths below 1000 nm. Light engine optics taken from a digital projector (NEC HT1000) serve to homogenize and direct the light onto a 0.7 in digital micromirror device (DMD Discovery™ 1100 with ALP Accessory Package, ViALUX, Germany). Grayscale spatial sinusoid patterns are projected at 400 Hz using the ViALUX software development toolkit, which generates the necessary pulse-width modulation of binary sub-frames to produce a specified grayscale bit-depth (1–8 bits). Finally, a fixed focal length (f = 100 mm) projection lens illuminates the tissue at a slight angle from normal with a 15 × 25 mm illumination field. Detection was performed at normal incidence using a CRI Nuance™ camera system, which combines a 12-bit CCD camera and a liquid crystal tunable filter (LCTF; λ = 650–1100 nm, Δλ = 10 nm). To avoid specular reflection, crossed linear polarizers are used in the illumination and detection arms. For this system, the former is a 1.5 in diameter NIR linear polarizer (Meadowlark Optics, VLM-200-IR-R) placed immediately after the projection lens, and the first stage of the Nuance LCTF serves as the latter. The DMD, CCD, and LCTF are controlled via USB by a laptop computer, and synchronized using LabVIEW software (LabVIEW 8, National Instruments), enabling fast acquisition of a series of patterns with various spatial frequencies.

12.2.2. SFD Measurement, Calibration, and Modeling

A detailed description of SFD measurement, calibration, and diffusion modeling is provided by Cuccia [32]. In this work, we modeled diffuse reflectance using a transport-based White Monte Carlo (WMC) method [33,34]. Previously, we have found that compared with Monte Carlo, (1) diffusion predictions over- and underestimate low- and high-

frequency diffuse reflectance, respectively, and (2) the quantitative accuracy of diffusion degrades with decreasing albedo [32]. Due to the moderate albedo of brain tissue ($\mu_s'/\mu_a \sim$ 10–20), we chose to analyze all brain data with the WMC approach. This homogeneous tissue model is a significant simplification of the multilayered rat brain, and more work is necessary to accurately model this complex system. We discuss further the consequences of our simple model in Section 12.2.5.

12.2.3. Optical Property Inversion Methods

In this chapter, we use two inversion methods to calculate the absorption and reduced scattering from measurements of diffuse reflectance. When high measurement precision is desired, we use a "sweep" in spatial frequency space, producing an overdetermined set of diffuse reflectance measurements, which can be fitted to our WMC forward model predictions using least-squares minimization. This method is performed for all spatially averaged region analysis of optical properties and chromophores. When increased acquisition and/or processing speed is desired, we alternatively use a rapid two-frequency lookup table method based on cubic spline interpolation [32]. This data can be achieved with a minimal 3-phase, single frequency image set (by demodulating and averaging the images to obtain AC and DC amplitude maps, respectively). On typical personal computers this approach is capable of millions of inverse lookup calculations per second, and is therefore used to calculate all high-resolution images including time sequences. The signal-to-noise ratio (and thus the measurement precision) of either approach is limited by the data sampling, with the two-frequency method having a lower precision with the tradeoff of higher acquisition and processing speed.

12.2.4. Spectral Analysis-Chromophore Calculation

The quantitative absorption coefficient is assumed to be a linear (Beer's law) summation of individual chromophore absorption contributions:

$$\mu_a(\lambda) = 2.303 \sum_{i=1}^{3} c_i \varepsilon_i(\lambda), \qquad \text{12.1}$$

where c_i and $\varepsilon_i(\lambda)$ represent chromophore concentrations and molar extinction coefficients, respectively. Using reported extinction coefficients of HbO$_2$/HbR35 and H$_2$O,36 we can invert Equation 12.1 and calculate tissue chromophore concentration separately at each pixel by linear least-squares fitting to the multispectral absorption images. Total hemoglobin (HbT) and oxygen saturation (S$_t$O$_2$) can then be calculated as HbT = HbR + HbO$_2$ and S$_t$O$_2$= HbO$_2$/(HbR + HbO$_2$) * 100, respectively.

12.2.5. Optical Property Mapping: Resolution Versus Quantitation

On a pixel-by-pixel basis, diffuse reflectance versus spatial frequency is fitted to the WMC forward model to extract the local absorption and reduced scattering optical property contrast. This process is repeated for each wavelength, resulting in multi-spectral absorption and scattering spectra at each pixel. The measured contrast from discrete absorbers and scatterers on millimeter and submillimeter spatial scales, however, will possess partial volume effects in all three spatial dimensions. This is due to the physical light transport length scales in tissue, limiting the true x-y resolution of optical property contrast to many detector pixels [32]. This phenomenon is not unique to MI, but present in all planar reflectance imaging measurements of turbid media. Absorption and scattering are calculated using a homogeneous reflectance model, extracting a locally averaged sampling of optical property contrast. Based on simulations of the tissue MTF for varying optical properties [32], we expect the resulting image resolution to scale directly with the transport length, $l^* = (\mu_a + \mu_s')^{-1}$, and the spatial frequency of illumination. In this chapter, we place quantitative emphasis on *average* optical properties and chromophores measured over a field of view that is greater than l^*. Spatial maps and videos of these parameters are displayed and referred to as "contrast maps," with the caveat that high resolution features will exhibit degraded quantitative accuracy.

12.2.6. In Vivo Rat CSD Experiments

12.2.6.1. Animal Preparation

MI spectroscopy measurements were performed on an in vivo Wistar rat model with a thinned-skull preparation. All procedures were performed in accordance with approved IACUC protocol guidelines. The animals were anesthetized, placed in a stereotaxic frame, their skulls thinned and glass coverslip applied. This preparation is described in detail by Masino et al. [37] The resulting thinned skulls allowed direct imaging of the cortex over a 5×7 mm field-of-view (whisker barrel cortex, centered at the C2 location). In order to investigate the sensitivity of MI toward studying acute cortical injury, we induced cortical spreading depression (CSD) by applying 1 M KCl solution to the surface of the cortex through a perforated section of skull and dura, located approximately 3 mm above the camera's imaging field.

12.2.6.2. MI Measurement Protocol

For each of three animals, our MI measurement protocol was twofold. Prior to CSD induction, baseline spatial modulation data were acquired at 6 spatial frequencies (3-phase projections each) from 0 to 0.26 mm^{-1}, at 10 nm intervals over the entire range between 650 and 980 nm. Depending on the wavelength, image acquisition times ranged from 200 ms to 4 s, with total spectral imaging time of approximately 30 s per spatial pattern. The entire measurement (34 wavelengths, 3 phases, 6 frequencies) was repeated three times for statistical averaging yielding an entire measurement time of approximately 30 min.

Next, rapid dynamic measurements were performed, beginning 1 min prior to K^+Cl^- administration. Here, a significantly reduced data set was chosen in order to achieve high temporal resolution. Two spatial frequencies (0 and 0.26 mm^{-1}) were acquired with three phase projection images, as described in Section 12.2.2, at each of four wavelengths (680, 730, 780, and 830 nm). The resulting 12 images took in total 6 s, permitting a repetition rate of 10 measurements per minute. The animals were followed for a period of 10 min for rats 1 and 2, and a period of 30 min for rat 3.

All images in this study were smoothed by 2D convolution with a Gaussian filter function (FWHM = 3 pixels), and baseline repetitions were averaged prior to data processing. Additionally, time-series data were post-processed by smoothing slightly in time (Gaussian FWHM of 2 timepoints = 12 s).

12.2.6.3. Spatial Frequency Sensitivity Analysis

Because of the differential absorption sensitivity at low and high frequencies, optimal optical property separation is achieved when a large range of frequencies is used [31]. In Figure 12.2a, we depict this differential sensitivity using diffuse reflectance (MTF) predictions versus frequency, increasing μ_a by 100% from 0.02 (black line) to 0.04mm^{-1} (gray line). This is done for two values of μ_s', 0.6 (solid lines) to 1.2mm^{-1} (dashed lines), simulating a 100% change in scattering. Notice that the low frequencies have a significant reflectance change due to absorption, while high frequency reflectance remains nearly unchanged. Conversely, reflectance changes due to scattering are observed at all spatial frequencies. In Figure 12.2b, we further visualize this by plotting the reflectance sensitivity to 1% changes in absorption and scattering. Whereas DC reflectance is equivalently sensitive to a fractional change in either absorption or scattering, at high spatial frequencies absorption contrast is lost while scattering contrast is retained. For instance, notice that at our maximum measurement frequency of 0.26 mm^{-1} the reflectance is roughly 24 times more sensitive to scattering compared to absorption ($\Delta R_d = 0.56 \ \mu_s'$ versus $0.024 * 10^{-3}$ for μ_a). This plays an important role in Section 12.3.2 during our discussion of dynamic scattering measurement.

In realistic heterogeneous tissues, a tradeoff exists between maximizing the frequency range for optical property accuracy and obtaining similar sampling volumes. As tissue is a low-pass spatial filter, high frequencies are attenuated quickly with depth. Using diffusion-based forward modeling, we have estimated mean sampling depths at 650 nm using measured average background optical properties of brain tissue. This was done by predicting the depth sensitivity to contrast from a planar perturbation in absorption, given a background fluence profile from spatial frequencies 0 and 0.26 mm^{-1}. Based on these results, we observe qualitatively similar depth sampling, with mean depth sampling ranging

between 2.5 mm and 1.2 mm (for $f_x = 0$ and 0.26 mm^{-1}, respectively). In all cases maximal sensitivity was found in the first 1–2 mm, where cortical hemodynamic changes occur.

12.3. RESULTS AND DISCUSSION

12.3.1. Baseline MI Spectroscopy

In Figure 12.3a we show a grayscale planar reflectance image of the cortical region of rat 1 at 650 nm. A dotted-line box denotes the region-of-interest (ROI) used for analysis, selected for its uniform illumination and the absence of cerebral bruising. The Monte Carlo-model fitting of spatial frequency data allows calculation of the absorption and reduced scattering coefficients. In Figure 12.3b we show the spatially averaged diffuse reflectance at 650 nm and the corresponding multi-frequency fit. Excellent agreement is observed between measurement data and the model-based fit, with derived μ_a and μ_s' coefficients of 0.033 and 0.70 mm^{-1}, respectively.

Analysis of multifrequency reflectance data separately at each pixel results in spatial maps of absorption and reduced scattering contrast. In Figure 12.3c, we plot the μa and $\mu s'$ maps recovered at 650 nm for rat 1. Note the strong absorption in the vein region, due to a large absorption by HbR at this wavelength. Below the images, we show histogram distributions of the corresponding quantitative maps above, indicating the degree of spatial variation in recovered optical properties. The mean and standard deviation for the pixel-wise μa and $\mu s'$ were 0.030 ± 0.007 mm^{-1} and 0.63 ± 0.13 mm^{-1}, respectively. These statistical results are in good agreement with the spatially averaged reflectance fit from Figure 12.3b, suggesting that our simple pixel-wise fitting approach yields optical properties similar to that calculated using a global analysis.

By mapping the absorption coefficient at multiple wavelengths, we can perform quantitative spectral imaging of tissue. In Figure 12.4, we summarize the baseline spectroscopy results for all three animals. In Figure 12.4a we show the μ_a (left) and μ_s' (right) coefficients versus wavelength (circles) recovered from spatially averaged fitting. Data for rat 1 is shown in black (rat 2 in dark gray; rat 3 in light gray). Note the distinct spectral features in absorption, resulting from oxy- and deoxy-hemoglobin (HbO$_2$, HbR), and water (H$_2$O) absorption. The calculated scattering coefficient generally decays with increasing wavelength, and the results from a power law ($\mu_s' = A \cdot \lambda(nm)^{-b}$, solid lines) fit are shown. A small residual coupling is observed between measured scattering and absorption spectral features. In particular, the scattering at the shortest and longest wavelengths appears to be underestimated by 5–10%, occurring where the corresponding absorption is highest (due to HbR and H$_2$O, absorption features, respectively). Based on our experiments in layered tissue phantoms [38], we believe this effect is primarily due to frequency-dependent probing volumes in the presence of depth-heterogeneous structures.

Simultaneous linear fitting of the absorption to known extinction coefficients yields measures of chromophore concentration. Shown in Figure 12.4a, multispectral fitting (solid line) for rat 1 yields HbO$_2$, HbR, H$_2$O, HbT and S$_t$O$_2$ values of 56.3 μM, 33.2 μM, 63.9%, 89.6 μM, and 56.3%, respectively. Tabulated results of chromophore values for all three animals are shown in Figure 12.4b. Lipid absorption near 930 nm was not apparent in the μ_a spectrum, and when included in the spectral analysis was not found to significantly affect the results. The small absorption "bump" at 900–910 nm is an artifact of imperfect phantom calibration due to the presence of a sharp, strong silicone absorption peak that is present in the phantom.

We note that the solution for chromophore concentration is well-determined when the number of wavelengths is at least equal to the number of chromophores. Therefore, as few as two wavelengths can be used to separate HbO$_2$ and HbR (if a constant value of H$_2$O is assumed). Repeating the above analysis with 780 and 830 nm only (assuming H$_2$O = 65%) yields results for HbO$_2$ and HbR within 10% of those from full spectral fitting. Repeating the above analyses using a simple diffusion-based model provided qualitatively similar results for absorption and scattering spectra, but in general was found to overestimate the absorption coefficient by 10–25%.

Absorption spectra at each pixel can be separately analyzed to yield spatial maps of local HbO$_2$, HbR, and H$_2$O distribution, shown in Figure 12.5. Notice the high concentration of HbR over the large superficial draining vessel

(venous) regions, also reflected in the S_tO_2 image, highlighting the effect of tissue oxygen extraction. Conversely, notice that the high albedo regions with less structural detail are highly oxygenated, with S_tO_2 levels between 60 and 70%. Lastly, the H_2O map reveals a relatively homogeneous distribution of water.

12.3.2. Dynamic MI Spectroscopy of CSD

We performed measurements of CSD in each of the three rats, as described in Section 12.2.3. The results are presented as follows. We first present data for a single animal, choosing rat 3 for its long observation period of 30 minutes. Three ROIs are selected for analysis, and baseline MI spectroscopy results are reported for each of these regions. Next, the observed dynamic time courses of diffuse reflectance, optical properties, and chromophore concentrations are shown for each ROI. We then present the full spatio-temporal dynamic contrast data for rat 3 (2D + time) in the form of "snapshot" images.

Figure 12.6 summarizes the baseline spectroscopy measurements for rat 3. In Figure 12.6a, we show three regions of interest superimposed on the DC reflectance map, chosen to highlight three different characteristic temporal profiles observed within the field of view. In Figure 12.6b we show the baseline spectral fits for each of these regions, and in Figure 12.6c we tabulate the resulting calculated chromophore concentrations. In general, Region A (black) is a high albedo region lacking any large blood vessels, whereas Regions B (dark gray) and C (light gray) include high-absorption blood vessels and mild cerebral bruising from surgery. These differences are apparent in their recovered absorption spectra and fits, with on average 27% higher HbT, and 32% lower saturation in the vascular regions. Also, 7% higher H_2O is found in Regions B and C, which may indicate increased edema due to bruising.

In Figures 12.7–12.9 (for regions A–C, respectively), we present the temporal dynamics of CSD in each ROI of rat 3 as measured by MI. In part (a) of each figure, we plot the multispectral diffuse reflectance changes at $f_x = 0$ mm^{-1} (DC, top) and $f_x = 0.26$ mm^{-1} (AC, bottom). In part (b), we plot the recovered $\Delta\mu_a$ (top) and $\Delta\mu_s'$ (bottom) optical properties at each wavelength. While absolute values of diffuse reflectance and optical properties are measured separately at each time point, for visualization purposes all data are displayed as a change from that prior to KCl administration. Absolute optical property values at t = 0 (not shown) demonstrate excellent agreement (~5–10%) with full multifrequency baseline data.

Looking first at the reflectance time courses of Figure 12.7a (Region A), we see in general a series of three CSD events over the 30 minutes, with each transient event occurring for approximately 4.3 minutes. The first event occurs at minute 2.9 after KCl application, indicating an initial latency between the insult and the first resulting spreading depression wave. Reflectance contrast is present in both DC and AC frequency components, but with markedly different signatures. Generally, the DC time course shows a slow, gradual decay, punctuated by sharp, wavelength-dependent spikes/dips (for short/long wavelengths, respectively). Alternatively, the AC signature contains three sets of transient dips consistent across all wavelengths, with final values leveling off progressively lower than baseline. Discussed in detail in the following paragraph, we believe these AC changes are due primarily a result of optical scattering and may be related to neuronal depolarization. The corresponding derived optical properties in Figure 12.7b reflects this, with μ_s' trends tracking directly with the measured AC reflectance. As expected, μ_a trends reveal similar wavelength-dependence of the DC reflectance (with opposite polarity), reflecting changes in HbO_2 and HbR.

In Section 12.2.3.3 we noted that the diffuse reflectance at $f_x = 0.26$ mm^{-1} is 23 times more sensitive to scattering changes compared to absorption. In this context, we propose that the observed magnitude of the CSD-induced AC reflectance changes can only be explained by changes in optical scattering. To concretely illustrate this point, we pick as an example the observed 780 nm AC diffuse reflectance dip in Figure 12.7a at t = 3.7 min of -0.003. Here, the corresponding change in reduced scattering in Figure 12.7b, $\Delta\mu_s'$, is calculated to be -0.03 mm^{-1}. In order for this change to instead be due to an absorption-only event, μ_a would need to increase by 121% from baseline (from 0.038 to 0.084 mm^{-1}). This increase would also need to be accompanied by a drop in R_d ($f_x = 0$ mm^{-1}) of 0.12 (33%), whereas the *actual* observed DC reflectance only drops by 0.008 (<1%) and thus cannot explain the change. Secondly, we note that the three sets of AC reflectance dips occur consistently across all four wavelengths. While an approximate 120%

increase in HbT could induce this decrease at high frequency, it would also require a large broad-wavelength decrease in the DC reflectance. We instead observe during these events that the DC increases at short wavelengths while the DC decreases at long wavelengths, suggesting primarily an exchange between HbO_2 and HbR volume fractions, as opposed to a dramatic HbT change.

Regions A–C (Figures 12.7–12.9) were chosen to highlight three different time signatures observed in the field of view during the CSD dynamics. The most contrasting feature between all three regions is the measured AC reflectance and the derived scattering coefficient. In Region B (Figure 12.8), each CSD event appears to cause a biphasic scattering change, with a sharp increase and then decrease, whereas a monophasic dip was observed in Region A (Figure 12.7). Region C (Figure 12.9) appears even more complex with a triphasic rise-dip-rise temporal profile. We observe that Regions A to C are located with increasing proximity to the CSD induction point (3 mm above the imaging field).

Because fractional changes in scattering and absorption have an equal (and opposite) effect on DC reflectance (see Section 12.2.3.3), any scattering (i.e., pathlength) changes measured here could be misinterpreted as absorption events with traditional ISOI analyses (i.e., DC reflectance only). In our observations, the measured scattering change of up to -0.05 mm^{-1} would be interpreted as an increase in absorption of up to $+0.005$ mm^{-1}, more than the maximum measured absorption change for wavelengths 730, 780, or 830 nm in any of the three regions. In order to account for differential pathlength changes, Kohl et al. proposed a multispectral model [39], which they used to differentiate dynamic scattering and absorption changes using ISOI. This approach improves ISOI accuracy, and has been generally adopted as the method of choice for quantitative functional imaging. For dynamic measurements, we see MI as an improvement over this approach as it alternatively uses frequency domain measurements at a single wavelength to derive absolute scattering and absorption coefficients. This potentially provides a simplified single-wavelength measurement apparatus for detection of scattering, and also avoids potential mis-estimation of background optical properties.

Light scattering changes induced by spreading depression have been reported previously, and a comprehensive review is provided by Somjen. With in vivo spatially resolved reflectance measurements, Kohl et al. [11] separated absorption from scattering and observed a biphasic scattering response similar to that of Region A. With simultaneous laser scattering and electrophysiological measurements, both Jarvis et al. and Tao et al. found a strong correlation between electrical and optical scattering changes [12,13,40]. Tao et al. noted spatial heterogeneity in the dynamic spreading depression (SD) waveform related to the proximity to the SD induction site, similar to our results.

Using linear spectral analysis of absorption at all four wavelengths, we calculated the time-dependent chromophore concentration for Regions A, B, and C, presented in Figure 12.10A,B,C, respectively. In each region, the calculated baseline concentrations of H_2O were assumed to be constant. All three regions exhibit remarkably similar trends in HbR, HbO_2, HbT, and S_tO_2. This similarity is not clear in the DC traces of Figures 12.7–12.9, further highlighting the benefit of accurate separation of μa and $\mu s'$. Focusing on the first CSD event, there is a very consistent signature of: (1) a 2-minute latency post-KCl administration, (2) a 30-second period of decreasing S_tO_2 (3) a dramatic spike in both S_tO_2 (3–10%) and HbT (2–4 μM) with rise and decay times of approximately 1 minute each. For each region, the final S_tO_2 is approximately 5–10% lower than baseline, while the HbT restores to baseline values. This process repeats again twice more, except that the phase (2) desaturation appears to be absent. Additionally, in the "vessel" Region 3, we observe a gradual increase in HbT over the 30 minutes, indicating chronic blood pooling.

We show in Figure 12.11 the spatio-temporal evolution of both chromophore concentration and scattering changes from the first SD wave in rat 3. These are depicted in the form of a time derivative, i.e., $(C(tn + 1) - C(tn))/(tn + 1 - tn)$, where C represents concentration/saturation/scattering values and tn represents time of acquisition for data point n. This visualization is appealing as it highlights the changes with high contrast [18]. From left to right, we show HbO_2, HbR, HbT, S_tO_2, and μ_s'. Notice the wave in scattering which propagates from top right to bottom left, at a rate of approximately 3 mm/min. An increase, or "spike" in scattering is observed initially in the top right hand corner, in close proximity to the location of KCl administration. Note the large spikes in HbT and S_tO_2 due to vascular activity from depression wave propagation through the measurement field. We observe a transient increase in saturation and blood volume. Over the longer time periods, however, we observe a slow, sustained trend toward hypoxia in the vein regions.

The spatio-temporal evolution of the scattering coefficient in Figure 12.11 reveals a spatially defined scattering wave (reduction in $\mu s'$) that precedes hemodynamic changes. The scattering drop is presumed to be a consequence of neuronal depolarization accompanying CSD. This observed wave pattern has been shown previously with reflectance ISOI and attributed to blood volume changes [18]. Interestingly, the scattering depolarization wave is clearly followed in space and time by the increase in deoxyhemoglobin (HbR), decrease in saturation (S_tO_2), and drop in oxyhemoglobin (HbO_2); changes that are consistent with depolarization-induced neural tissue oxygen consumption.

12.3.3. Dynamic MI Spectroscopy of Stroke

In order to assess the sensitivity of MI to stroke, we conducted preliminary studies in a rat middle cerebral artery occlusion (MCAo) model, the most commonly involved artery in ischemic strokes. The left MCA was surgically cauterized using monopolar cautery or ligated to produce a permanent stroke. Figure 12.12 shows pre-versus post-MCAo results for a representative animal. Data were acquired at 5 wavelengths, 680, 800, 880, 920, and 980 nm in 3-minute intervals, and data points displayed every 6 minutes. Values for hemoglobin and saturation parameters were calculated from wavelength-dependent optical properties for each pixel, then averaged over the entire field of view (2 mm × 2 mm, 200 × 200 pixels) in the left hemisphere.

Stable baseline values for hemoglobin and S_tO_2 were measured for 27 minutes prior to MCAo. Dynamic changes were observed for each parameter within the first ~20 minutes of stroke and stabilized shortly thereafter with no significant variation between approximately 21 and 45 minutes post MCAo. The lack of new oxygenated blood supply following stroke resulted in a significant decrease in HbO_2 from ~50 µM to ~22 µM. In order to meet tissue metabolic demands, HbR was commensurately elevated from ~35 µM to ~49 µM due to oxygen extraction by ischemic neural tissues. This significant metabolic effect is also revealed by the dramatic drop in tissue saturation (S_tO_2) from baseline levels of ~60% to 30% after injury. Total hemoglobin (HbT), which roughly corresponds to blood flow, drops from 90 µM to 70 µM.

These results confirm previous observations of hemodynamic changes during cerebral ischemia in a rat model using diffuse optical tomography (DOT) [41] and multispectral reflectance imaging [42]. Although we report spatially-averaged cortical values in Figure 12.12, the MI technique also generates maps of cortical properties, making it a relatively simple approach for assessing hemodynamic and metabolic changes from different regions of the brain. For example, the S_tO_2 image for the same animal, shown in Figure 12.13, reveals uniform, low contrast tissue saturation levels of ~60% prior to MCAo. Twenty-five minutes following MCAo, clear spatial variations in S_tO_2 emerge, including the appearance of a high-contrast venous region where S_tO_2 values drop to ~20%. This strong tissue desaturation is a consequence of stroke-induced reductions in HbO_2 supply, accompanied by an increase in HbR as active neural tissue extracts oxygen. Similar spatio-temporal variations can be mapped and coregistered for all tissue chromophores.

12.4. CONCLUSION AND FUTURE DIRECTIONS

In conclusion we have presented a new method for quantitatively mapping tissue absorption and scattering properties, thereby allowing local sampling of in vivo concentrations of oxy- and deoxy-hemoglobin in CSD and stroke models of brain injury. Consistent dynamic changes in both scattering and absorption highlight the importance of optical property separation for quantitative assessment of tissue hemodynamics. Overall, these results demonstrate that MI can provide additional information content that enhances conventional ISOI methods. Future work involves further measurement of stroke and trauma, as well as epilepsy, migraine, and neuroplasticity. With continued technology development to optimize speed and spectral content, and advances in model-based reconstructions of tissue optical and physiological properties, we anticipate that the general platform of spatially modulated structured illumination can be easily integrated and coregistered with additional wide-field methods such as speckle correlation and fluorescence. In addition, MI can be used clinically in an intraoperative setting to provide feedback and guidance for surgeons. Because structured light introduces unique spatial and temporal selectivity, we expect that this approach will ultimately allow us to develop truly multidimensional methods for 3D tomography of neural tissue composition and metabolism.

ACKNOWLEDGMENTS

REFERENCES

1. Pierce M, et al. Advances in optical coherence tomography imaging for dermatology. J. Investigative Dermatol. 2004;123(3):458–463. [PubMed: 15304083]
2. NHLBI Working Group. Meeting Note: Cerebrovascular Biology and Disease. 2005
3. Zepeda A, C. Arias, F. Sengpiel Optical imaging of intrinsic signals: Recent developments in the methodology, its applications. J. Neurosci. Meth. 2004;136:1–21. [PubMed: 15126041]
4. Frostig RD, et al. Cortical functional architecture and local coupling between neuronal activity and the microcirculation revealed by in vivo high-resolution optical imaging of intrinsic signals. Proc Natl Acad Sci USA. 1990;87(16):6082–6086. [PMC free article: PMC54476] [PubMed: 2117272]
5. Grinvald A, et al. Functional architecture of cortex revealed by optical imaging of intrinsic signals. Nature. 1986;324(6095):361–364. [PubMed: 3785405]
6. Cohen LB, Changes in neuron structure during action potential propagation, synaptic transmission. Physiol Rev. 1973;53(2):373–418. [PubMed: 4349816]
7. Somjen GG, Mechanisms of spreading depression, hypoxic spreading depression-like depolarization. Physiol Rev. 2001;81(3):1065–1096. [PubMed: 11427692]
8. Narayan SM, E.M. Santori, A.W. Toga Mapping functional activity in rodent cortex using optical intrinsic signals. Cereb Cortex. 1994;4(2):195–204. [PubMed: 8038568]
9. Narayan SM, et al. Imaging optical reflectance in rodent barrel and forelimb sensory cortex. Neuroimage. 1994;1(3):181–90. [PubMed: 9343569]
10. O'Farrell AM, et al. Characterization of optical intrinsic signals and blood volume during cortical spreading depression. Neuroreport. 2000;11(10):2121–2125. [PubMed: 10923656]
11. Kohl M, et al. Separation of changes in light scattering and chromophore concentrations during cortical spreading depression in rats. Opt Lett. 1998;23(7):555–557. [PubMed: 18084575]
12. Tao L, Light scattering in brain slices measured with a photon counting fiber optic system. J Neurosci Methods. 2000;101(1):19–29. [PubMed: 10967358]
13. Tao L, et al. Light scattering in rat neocortical slices differs during spreading depression and ischemia. Brain Res. 2002;952(2):290–300. [PubMed: 12376191]
14. Jones M, J. Berwick, J. Mayhew, Changes in blood flow oxygenation, volume following extended stimulation of rodent barrel cortex. Neuroimage. 2002;15(3):474–487. [PubMed: 11848691]
15. Durduran T. Non-Invasive Measurements of Tissue Hemodynamics with Hybrid Diffuse Optical Methods. Dept of Physics and Astronomy, University of Pennsylvania; 2004.
16. Ayata C, et al. Pronounced hypoperfusion during spreading depression in mouse cortex. J Cereb Blood Flow Metab. 2004;24(10):1172–1182. [PubMed: 15529018]
17. Jones PB, et al. Proc SPIE Int Soc Opt Eng. Boston, MA: 2005. Multimodal optical imaging of mouse Ischemic cortex. Optical Methods in Drug Discovery and Development.
18. Chen S, et al. In vivo optical reflectance imaging of spreading depression waves in rat brain with and without focal cerebral ischemia. J Biomed Opt. 2006;11(3):34002. [PubMed: 16822052]
19. Chen S, et al. Time-varying spreading depression waves in rat cortex revealed by optical intrinsic signal imaging. Neurosci Lett. 2006;396(2):132–136. [PubMed: 16356631]
20. Ba AM, et al. Multiwavelength optical intrinsic signal imaging of cortical spreading depression. J Neurophysiol. 2002;88(5):2726–2735. [PubMed: 12424307]
21.

Yoon RS, et al. Characterization of cortical spreading depression by imaging of intrinsic optical signals. Neuroreport. 1996;7(15–17):2671–2674. [PubMed: 8981444]

22. Chen S, et al. Origin sites of spontaneous cortical spreading depression migrated during focal cerebral ischemia in rats. Neurosci Lett. 2006;403(3):266–270. [PubMed: 16737776]

23. Dunn AK, et al. Dynamic imaging of cerebral blood flow using laser speckle. J Cereb Blood Flow Metab. 2001;21(3):195–201. [PubMed: 11295873]

24. Bolay H, et al. Intrinsic brain activity triggers trigeminal meningeal afferents in a migraine model. Nat Med. 2002;8(2):136–42. [PubMed: 11821897]

25. Zepeda A, et al. Reorganization of visual cortical maps after focal ischemic lesions. J Cereb Blood Flow Metab. 2003;23(7):811–820. [PubMed: 12843784]

26. Manoonkitiwongsa PS, et al. Neuroprotection of ischemic brain by vascular endothelial growth factor is critically dependent on proper dosage and may be compromised by angiogenesis. J Cereb Blood Flow Metab. 2004;24(6):693–702. [PubMed: 15181377]

27. Jacques SL, Pogue BW. Tutorial on diffuse light transport. J Biomed Opt. 2008;13(4):041302. [PubMed: 19021310]

28. Zhou C, et al. Diffuse optical correlation tomography of cerebral blood flow during cortical spreading depression in rat brain. Opt Express. 2006;14:1125–1144. [PubMed: 19503435]

29. Bevilacqua F, et al. Broadband absorption spectroscopy in turbid media by combined frequency-domain and steady-state methods. Appl Opt. 2000;39(34):6498–6507. [PubMed: 18354663]

30. Cuccia DJ, et al. Modulated imaging: Quantitative analysis and tomography of turbid media in the spatial-frequency domain. Opt Lett. 2005;30(11):1354–1356. [PubMed: 15981531]

31. Cuccia DJ, et al. Quantitative recovery of tissue optical properties in the spatial frequency domain using modulated imaging. Optical Society of America Annual Meeting: Frontiers in Optics; Tucson, Arizona. 2005.

32. Cuccia DJ. Modulated Imaging: A Spatial Frequency Domain Imaging Method for Wide-field Spectroscopy and Tomography of Turbid Media in Biomedical Engineering. University of California; Irvine: 2006.

33. Kienle A, Patterson MA. Determination of the optical properties of turbid media from a single Monte Carlo simulation. Phys Med Biol. 1996;41:2221–2227. [PubMed: 8912392]

34. Swartling J, et al. Accelerated Monte Carlo models to simulate fluorescence spectra from layered tissues. J Opt Soc Am A Opt Image Sci Vis. 2003;20(4):714–727. [PubMed: 12683499]

35. Prahl S. Optical Absorption of Hemoglobin. Oregon Medical Laser Center; 1999. Website (http://omlc .ogi.edu/spectra/hemoglobin/index.html)

36. Hale GM, Querry MR. Optical constants of water in the 200 nm to 200 μm wavelength region. Appl Opt. 1973;12:555–563. [PubMed: 20125343]

37. Masino SA, et al. Characterization of functional organization within rat barrel cortex using intrinsic signal optical imaging through a thinned skull. Proc Natl Acad Sci USA. 1993;90(21):9998–10002. [PMC free article: PMC47700] [PubMed: 8234348]

38. Weber JR, et al. Towards Functional optical imaging in layered tissues using modulated imaging. Optical Society of America Annual BIOMED Topical Meeting; March 19–22, 2006; Ft. Lauderdale, FL.

39. Kohl M, et al. Physical model for the spectroscopic analysis of cortical intrinsic optical signals. Phys Med Biol. 2000;45(12):3749–3764. [PubMed: 11131197]

40. Jarvis CR, T.R. Anderson, R.D. Andrew Anoxic depolarization mediates acute damage independent of glutamate in neocortical brain slices. Cereb Cortex. 2001;11(3):249–259. [PubMed: 11230096]

41. J. P. Culver et al. Diffuse optical tomography of cerebral blood flow, oxygenation and metabolism in rat during focal ischemia. J Cereb Blood Flow Metab. 2003;23:911–924. [PubMed: 12902835]

42. Jones PB, et al. Simultaneous multispectral reflectance imaging and laser speckle flowmetry of cerebral blood flow and oxygen metabolism in focal cerebral ischemia. J Biomed Opt. 2008;13(4):044007. [PMC free article: PMC2790046] [PubMed: 19021335]
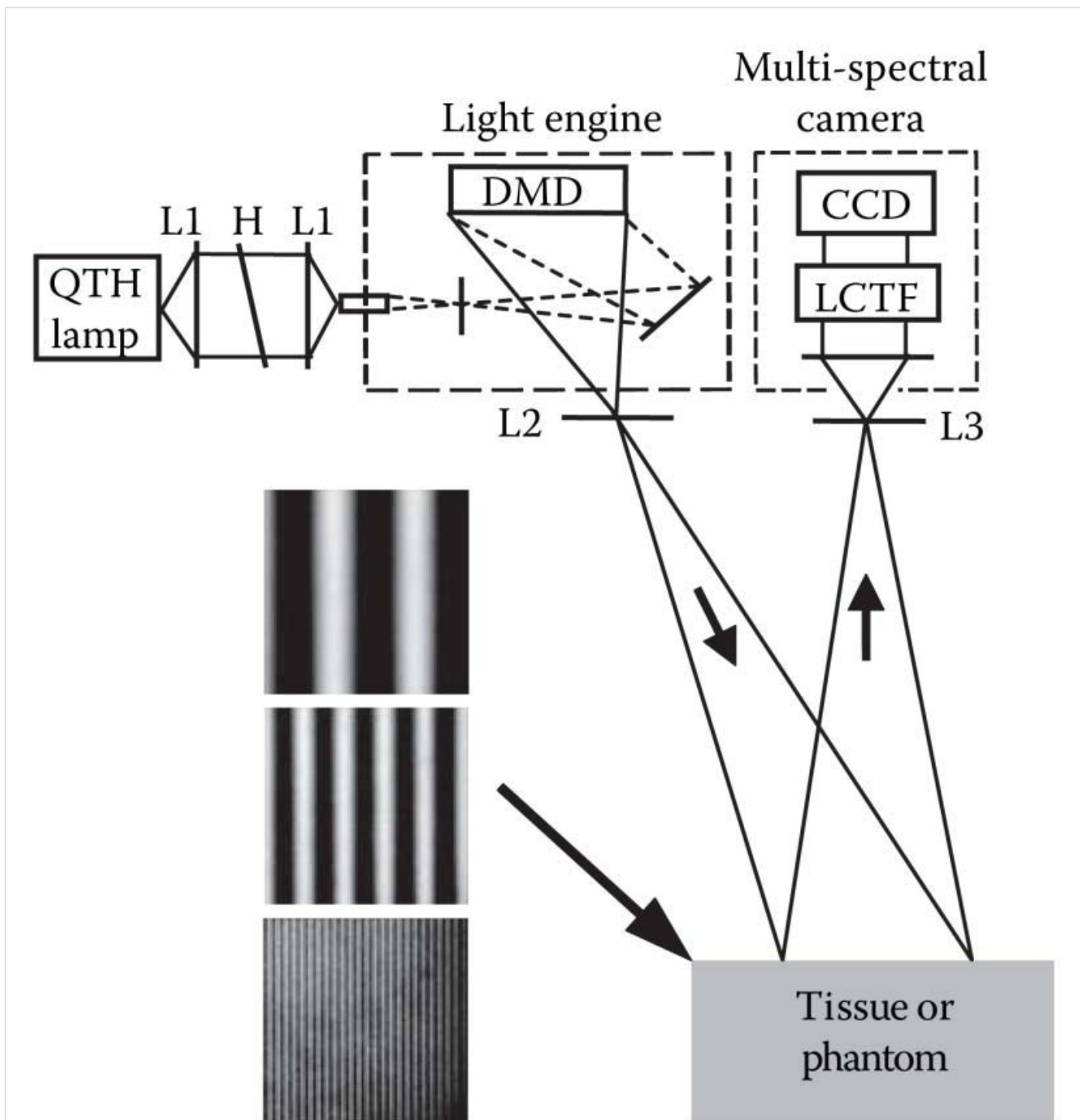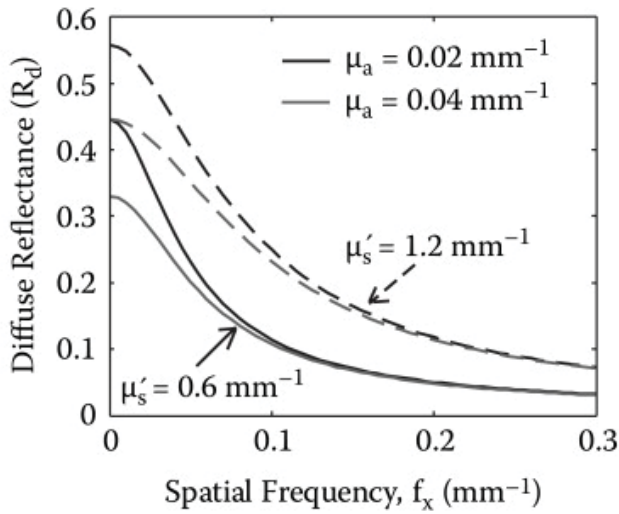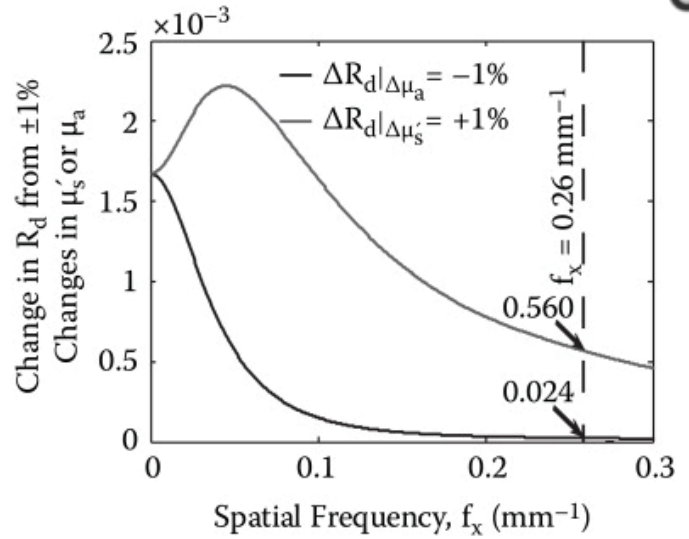
Figures

FIGURE 12.1

Modulated imaging platform. QTH—quartz tungsten halogen; L1—aspheric condenser; H—hybrid hot mirror; DMD—digital micromirror device; L2—projection lens; L3—camera lens; LCTF—liquid crystal tunable filter; CCD—charge-coupled device.
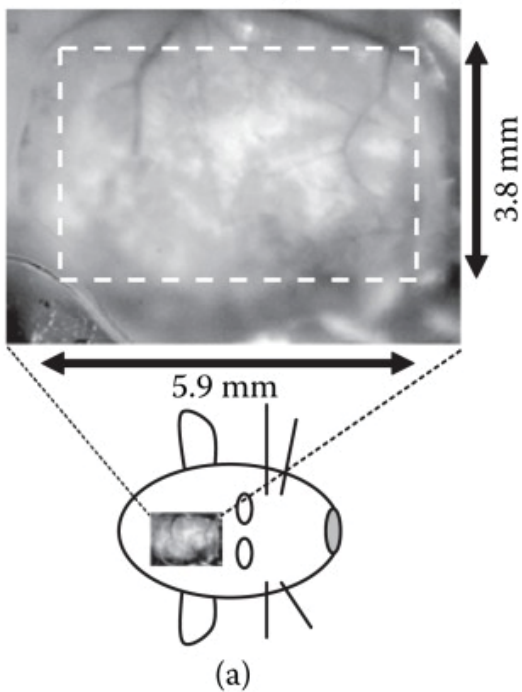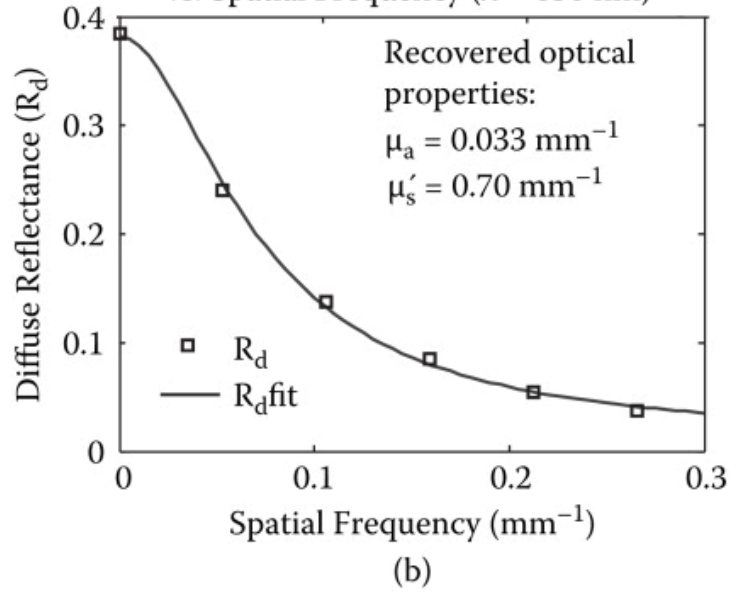
FIGURE 12.2

(a) Reflectance contrast in absorption and scattering covering a typical range of brain optical properties. (b) The frequency-dependent sensitivity to absorption (black line) and scattering (gray line), respectively. Reflectance at fx = 0.26 mm^{-1} is 24 times more sensitive to scattering contrast compared to that of absorption.

Rat 1–Baseline: Planar Diffuse Reflectance + ROI (λ = 650 nm)

3.8 mm

5.9 mm

(a)

Rat 1–Baseline: Average Diffuse Reflectance vs. Spatial Frequency (λ = 650 nm)

Recovered optical properties:
$\mu_a = 0.033$ mm^{-1}
$\mu_s' = 0.70$ mm^{-1}

$\square$ R_d
— $R_d$fit

Diffuse Reflectance (R_d)

Spatial Frequency (mm^{-1})

(b)

Rat 1–Baseline: μ_a Map and Histogram, 650 nm (mm^{-1})

Mean = 0.030 ± 0.007 mm^{-1}

Counts (×10^4)

μ_a' (mm^{-1})
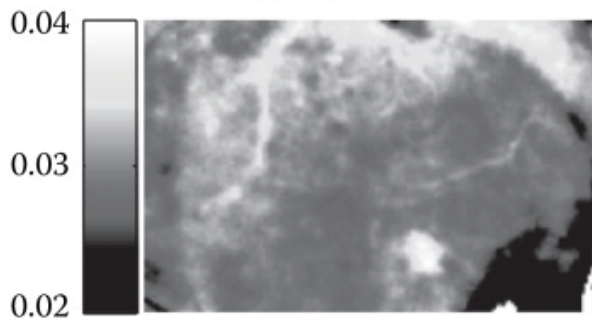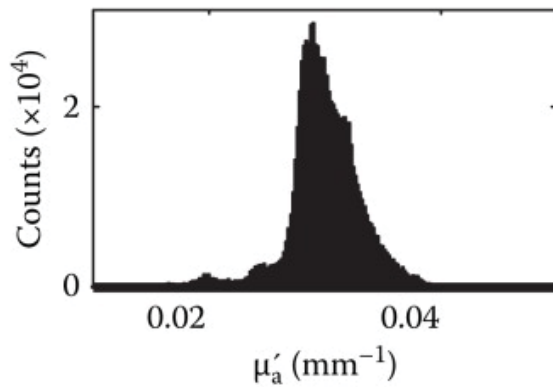
Rat 1–Baseline: μ_s' Map and Histogram, 650 nm (mm^{-1})

Mean = 0.63 ± 0.13 mm^{-1}

Counts (×10^4)

μ_s' (mm^{-1})
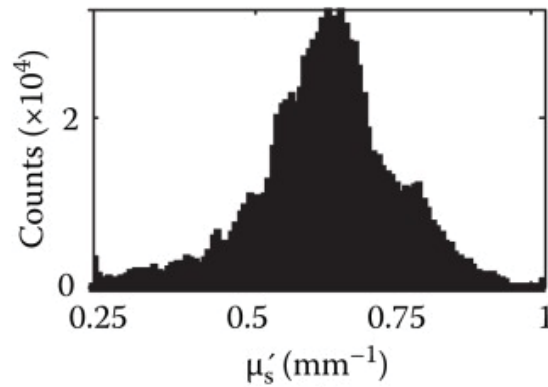
(c)

FIGURE 12.3

(a) Reflectance map for rat 1, showing the 3.8×5.9 mm region chosen for quantitative analysis. (b) Sample MTF reflectance data (squares) and fit (solid line) at 650 nm. (c) Recovered optical property maps (above) and corresponding image histogram over the analyzed ROI.

Rats 1-3–Baseline: Average μ_a and $\mu_{a,fit}$

Rats 1-3–Baseline: Average μ_s' and $\mu_{a,fit}'$

- $\circ/ - \mu_a/\mu_{a,fit}$ (Rat 1)
- $\circ/ - \mu_a/\mu_{a,fit}$ (Rat 2)
- $\circ/ - \mu_a/\mu_{a,fit}$ (Rat 3)

- $\circ/ - \mu_s'/\mu_{s,fit}'$ (Rat 1)
- $\circ/ - \mu_s'/\mu_{s,fit}'$ (Rat 2)
- $\circ/ - \mu_s'/\mu_{s,fit}'$ (Rat 3)

(a)
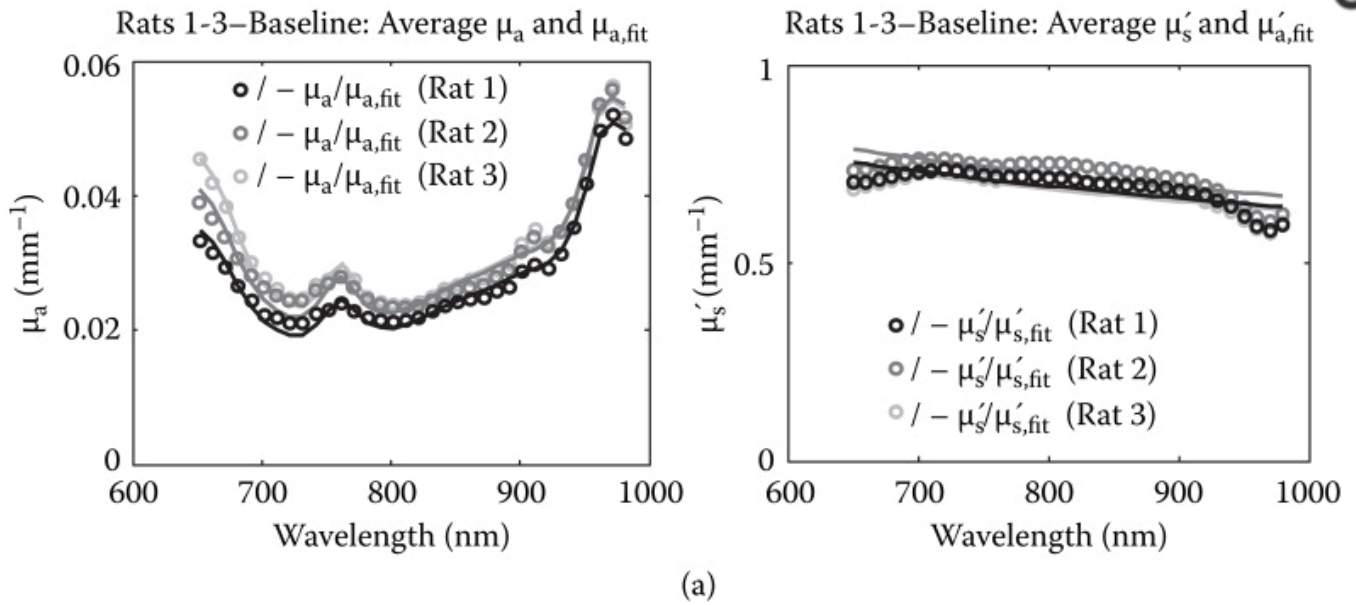
Rats 1-3–Baseline: Average Chromophore Fitting Results

Animal	HbO_2 (µM)	HbR (µM)	H_2O (%)	HbT (µM)	S_TO_2 (%)
Rat 1	56.3	33.2	63.9	89.6	62.9
Rat 2	59.6	39.7	67.9	99.3	60.0
Rat 3	57.6	45.7	67.4	103.3	55.8
Average	57.8	39.5	66.4	97.4	59.6
Std. Dev.	1.7	6.3	2.2	7.0	3.6

(b)

FIGURE 12.4

(a) Average μ_a (left) and μ_s'(right) spectra over entire ROI (circles). HbO_2, HbR, and H_2O concentrations are determined by subsequent least-squares fitting (solid lines) of molar extinction coefficients to the absorption. Data shown for rats 1 (blue), 2 (green), and 3 (red). (b) Tabulated results of chromophore values determined from spectral fitting.
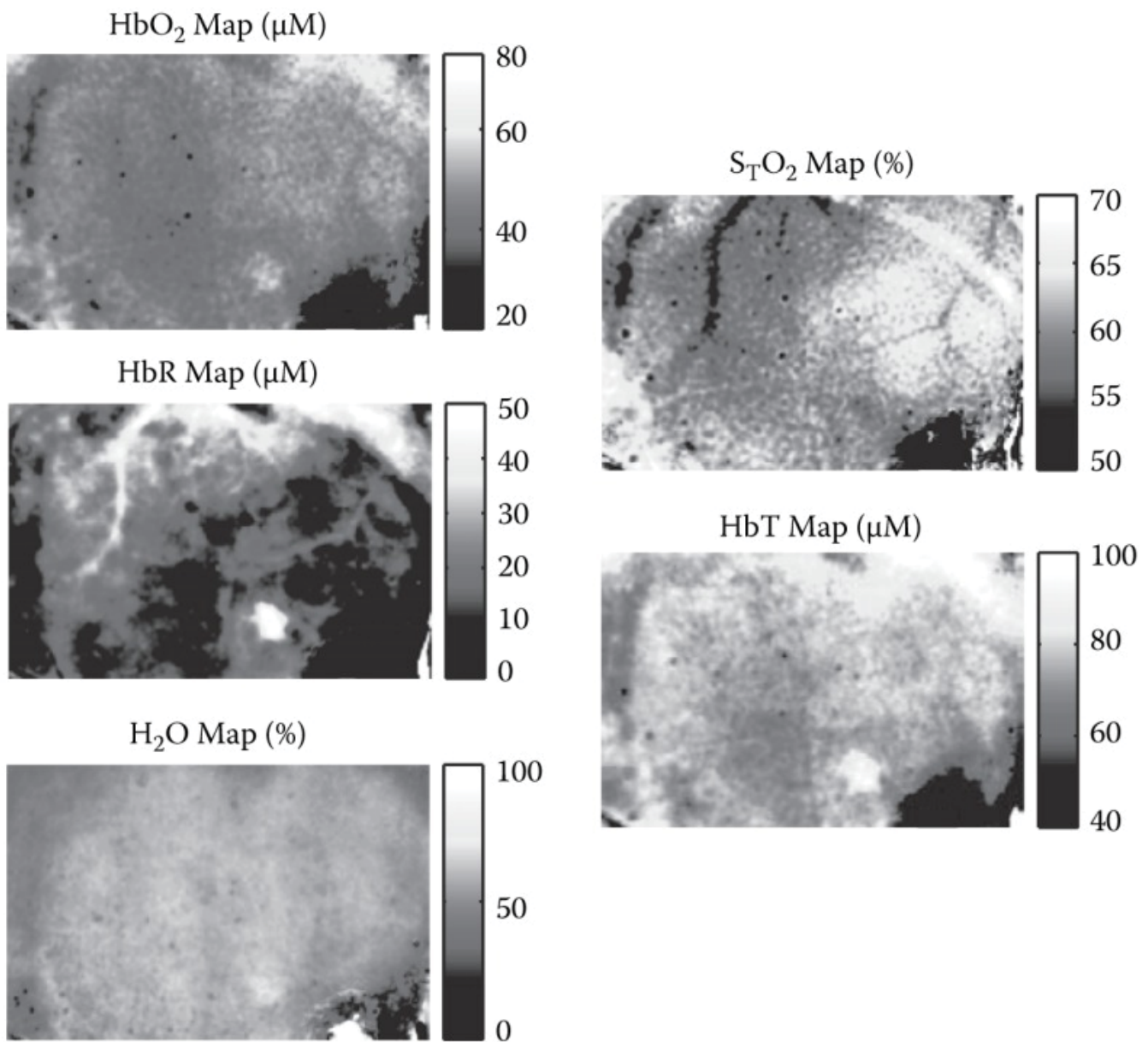
FIGURE 12.5

Chromophore fits to absorption spectra at each pixel yield maps of local HbO_2, HbR, and H_2O concentration (left). Total hemoglobin (HbT) and oxygen saturation (S_tO_2) maps can then be calculated from HbO_2 and HbR.

Rat 3–Baseline: Reflectance and ROIs

5 mm

7 mm

(A)

Rat 3–Baseline: μ_a and $\mu_{a,fit}$ in ROIs A-C

μ_a (mm^{-1})

o / – $\mu_a/\mu_{a,fit}$ (Region A)
o / – $\mu_a/\mu_{a,fit}$ (Region B)
o / – $\mu_a/\mu_{a,fit}$ (Region C)

Wavelength (nm)

(B)

Rat 3–Baseline: Chromophore Fits in ROIs A-C

Region	HbO$_2$ (μM)	HbR (μM)	H$_2$O (%)	HbT (μM)	S$_T$O$_2$ (%)
A	57.6	45.7	67.4	103.3	55.8
B	45.7	85.8	73.7	131.5	34.7
C	54.2	75.8	70.5	129.9	41.7
Average	52.5	69.1	70.5	121.6	44.1
Std. Dev.	6.1	20.9	3.2	15.8	10.7

(C)
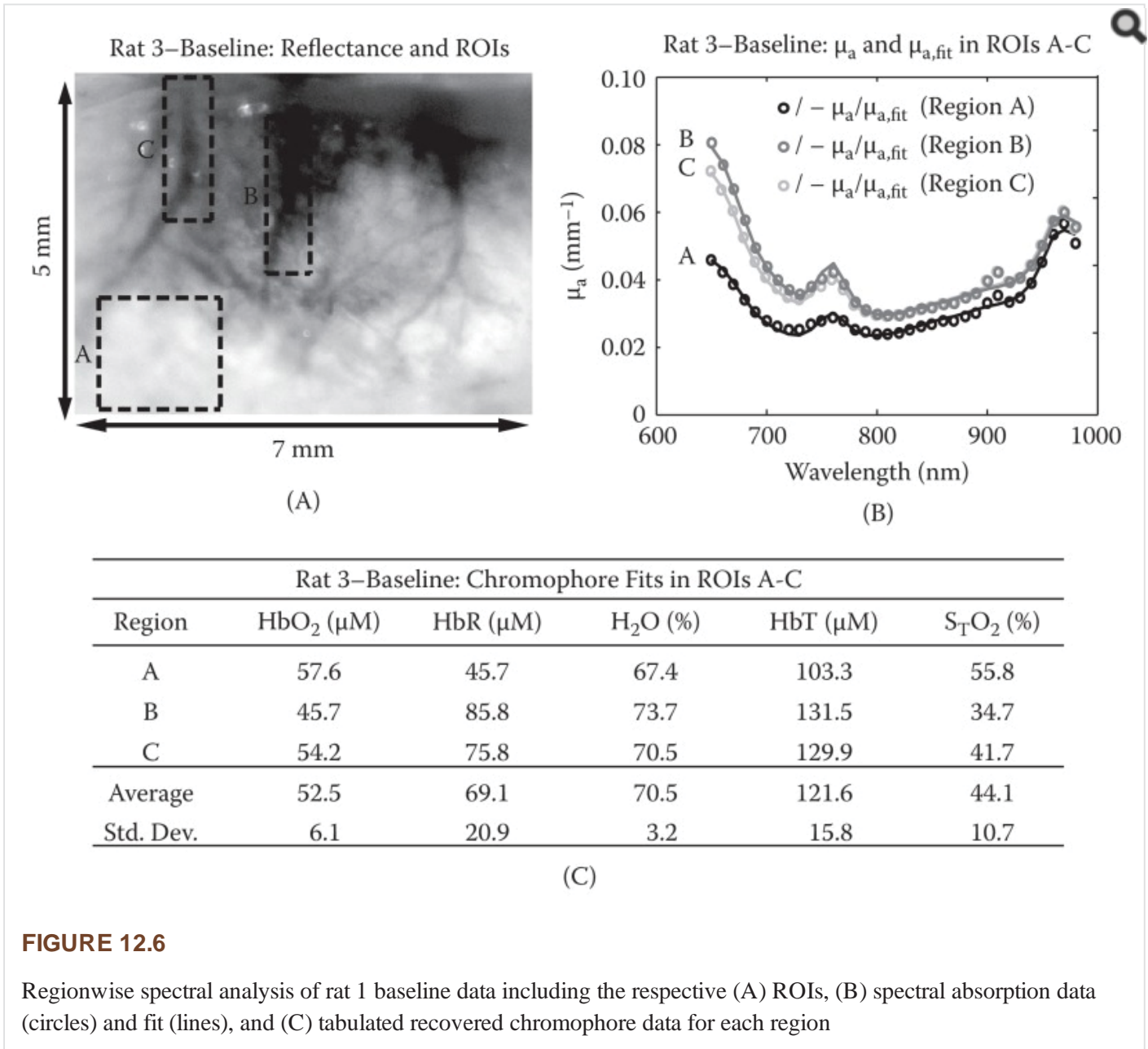
FIGURE 12.6

Regionwise spectral analysis of rat 1 baseline data including the respective (A) ROIs, (B) spectral absorption data (circles) and fit (lines), and (C) tabulated recovered chromophore data for each region

Rat 3–CSD: ΔDiffuse Reflectance (R_d) vs. Time
(Region A)

(A)
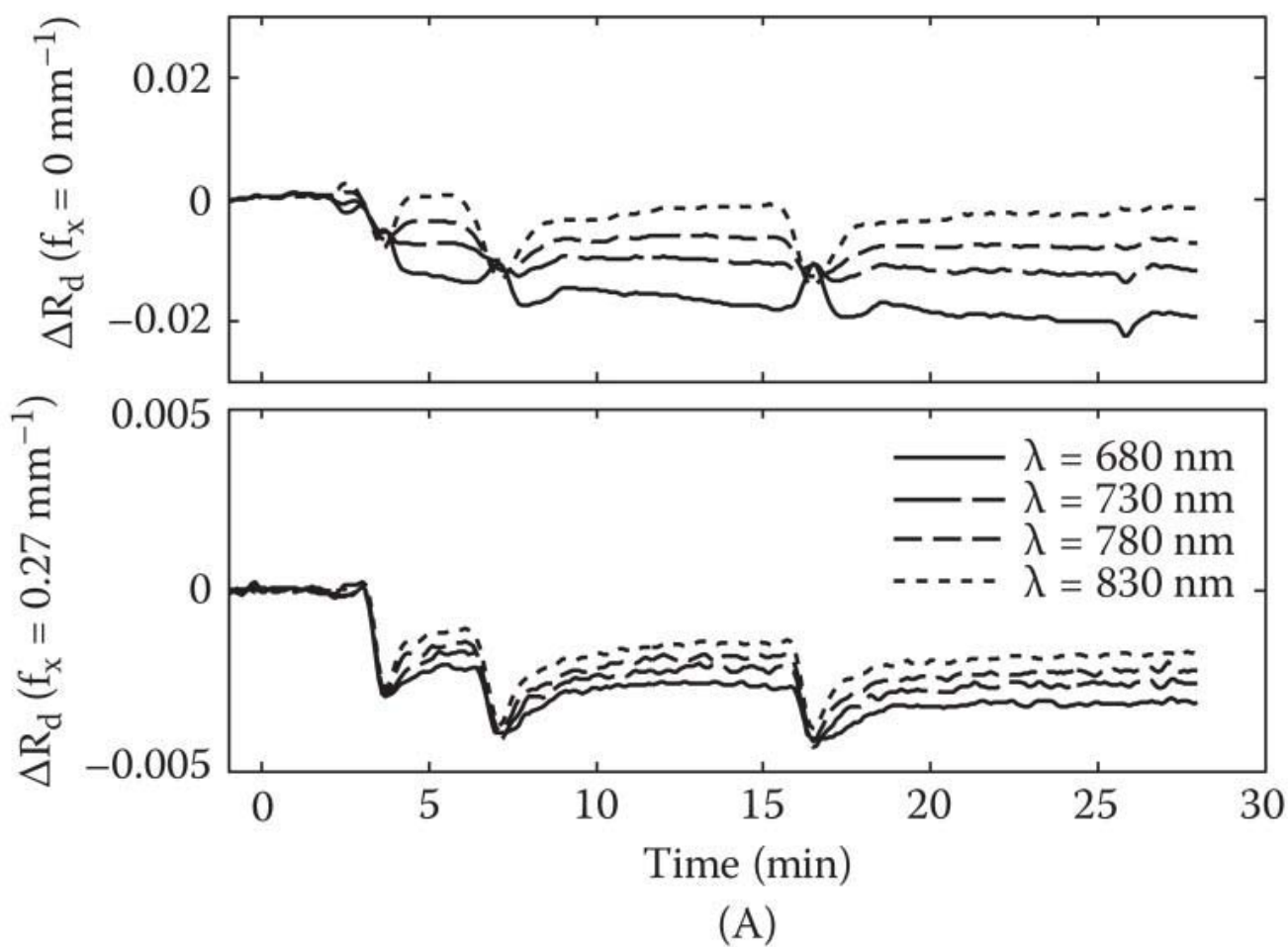
Rat 3–CSD: ΔOptical Properties (μ_a, μ_s') vs. Time
(Region A)
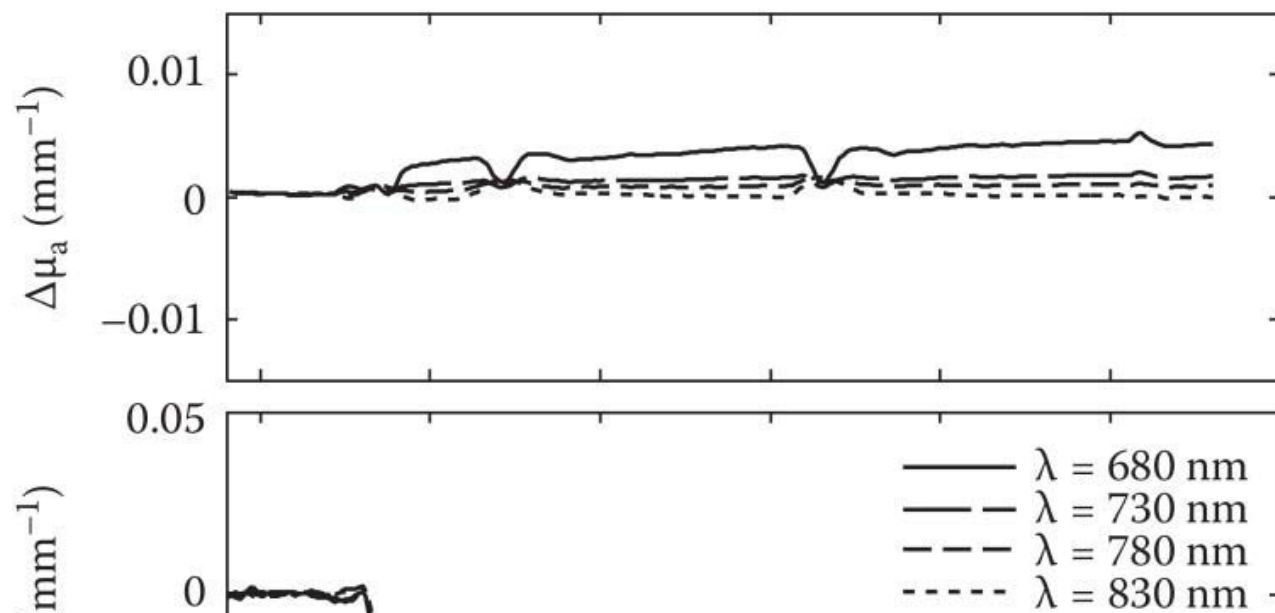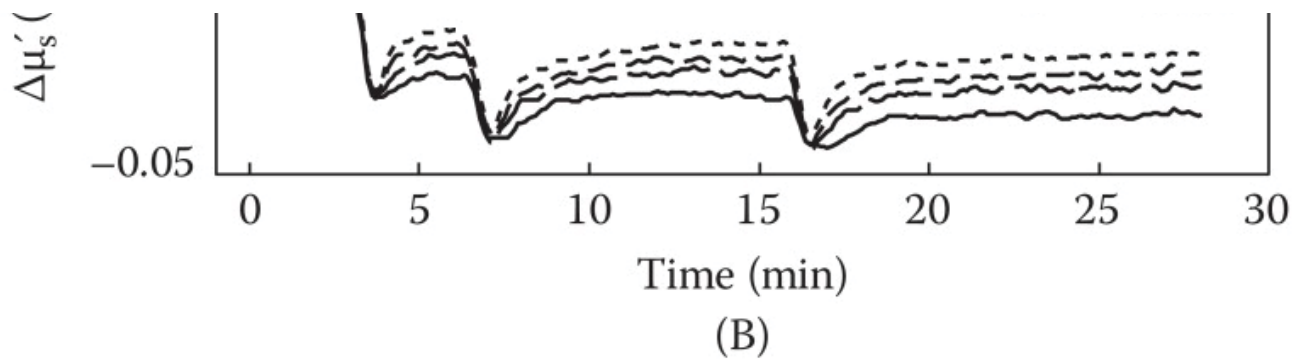
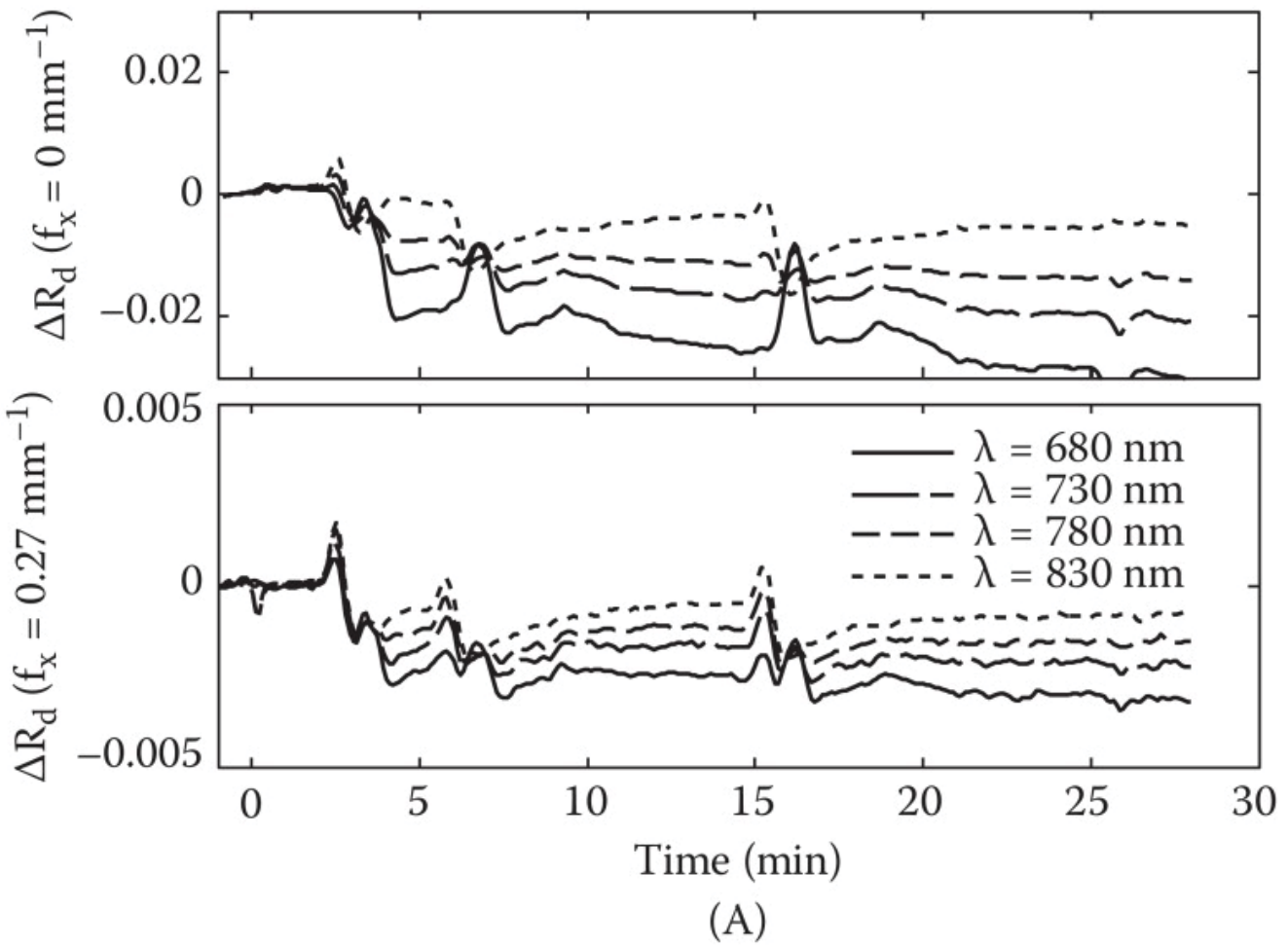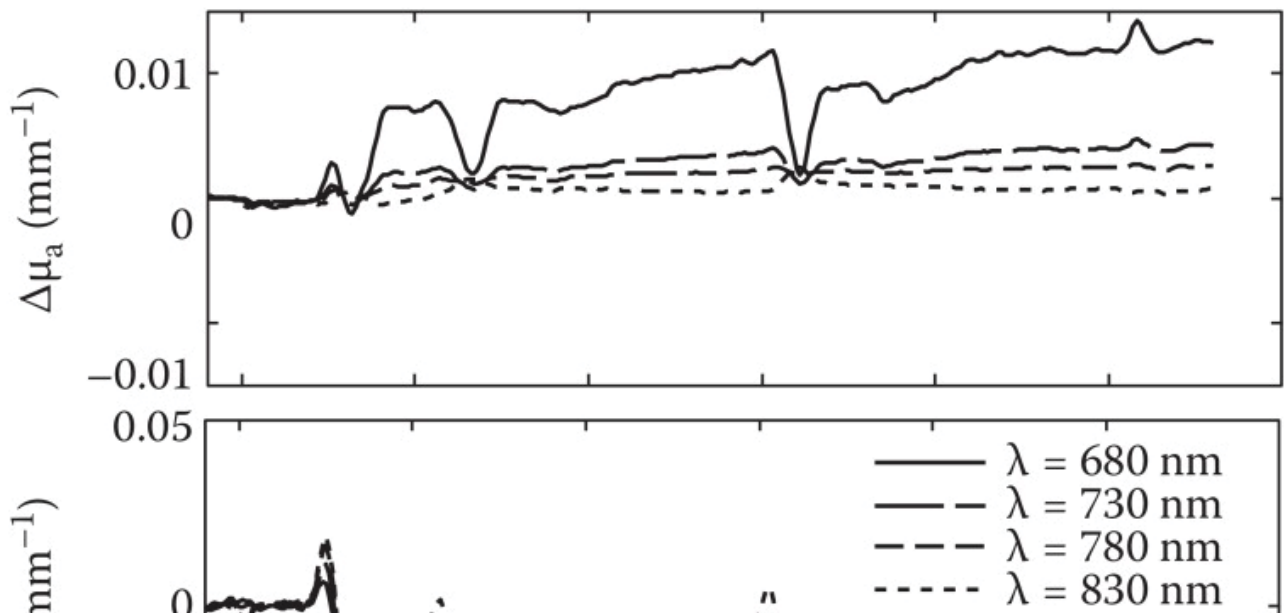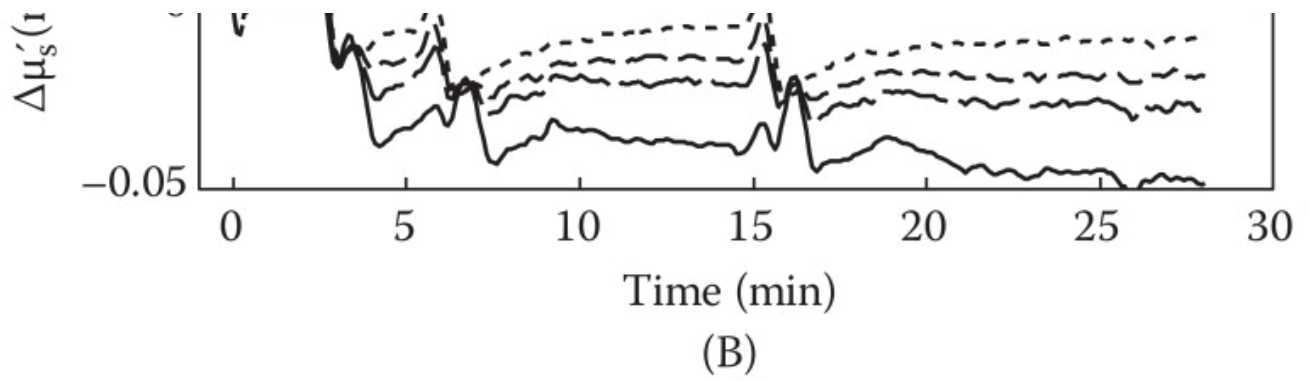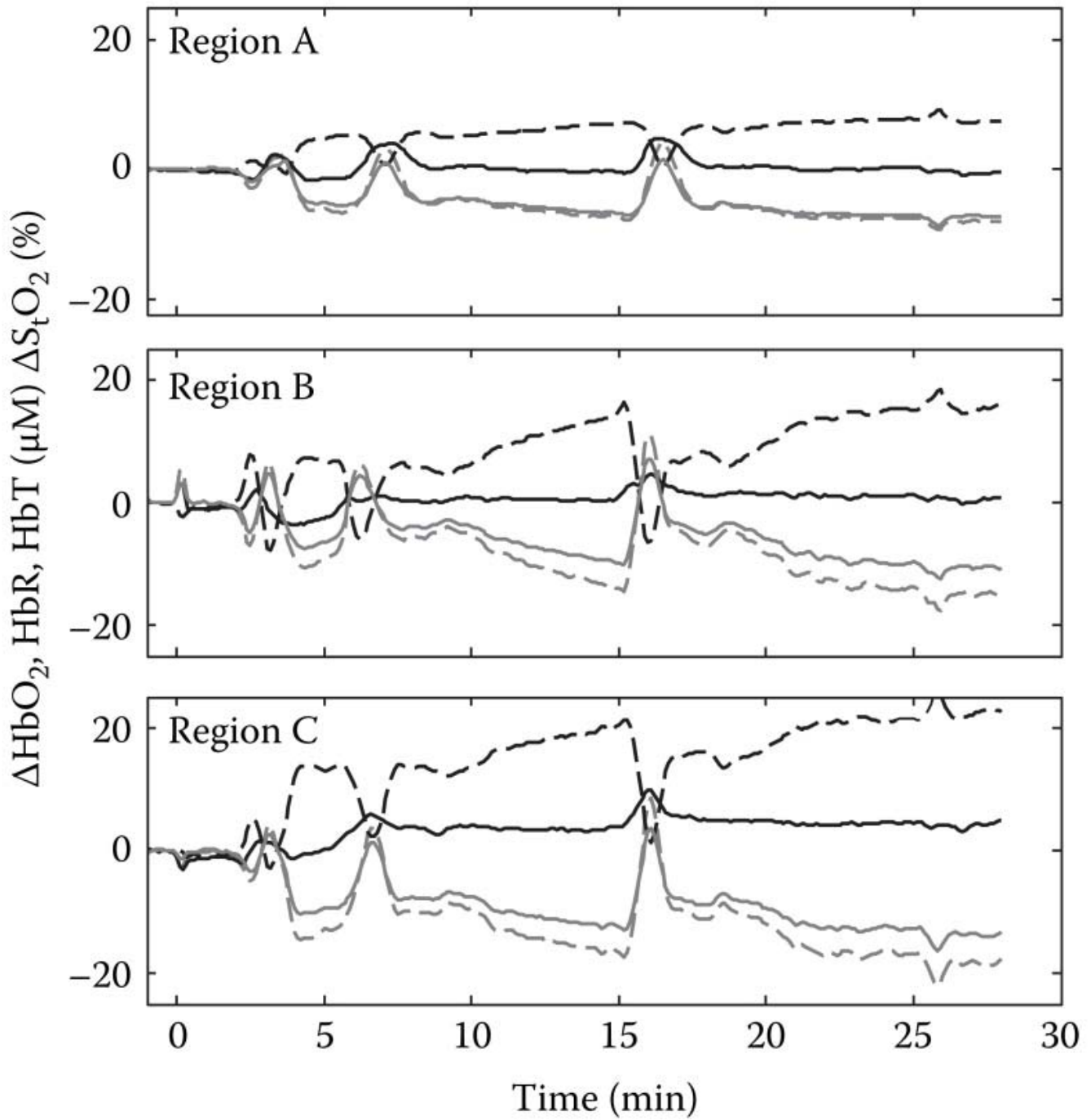**FIGURE 12.7**

(A) Multispectral diffuse reflectance at DC ($fx = 0$ mm^{-1}, top) and DC ($fx = .26$ mm^{-1}, bottom) for Region A of rat 3 over approximately 30 min. (B) Corresponding recovered multispectral absorption (top) and reduced scattering (bottom) coefficients.

Rat 3–CSD: ΔDiffuse Reflectance (R_d) vs. Time
(Region B)

$\lambda = 680$ nm
$\lambda = 730$ nm
$\lambda = 780$ nm
$\lambda = 830$ nm

(A)

Rat 3–CSD: ΔOptical Properties (μ_a, μ_s') vs. Time
(Region B)

$\lambda = 680$ nm
$\lambda = 730$ nm
$\lambda = 780$ nm
$\lambda = 830$ nm
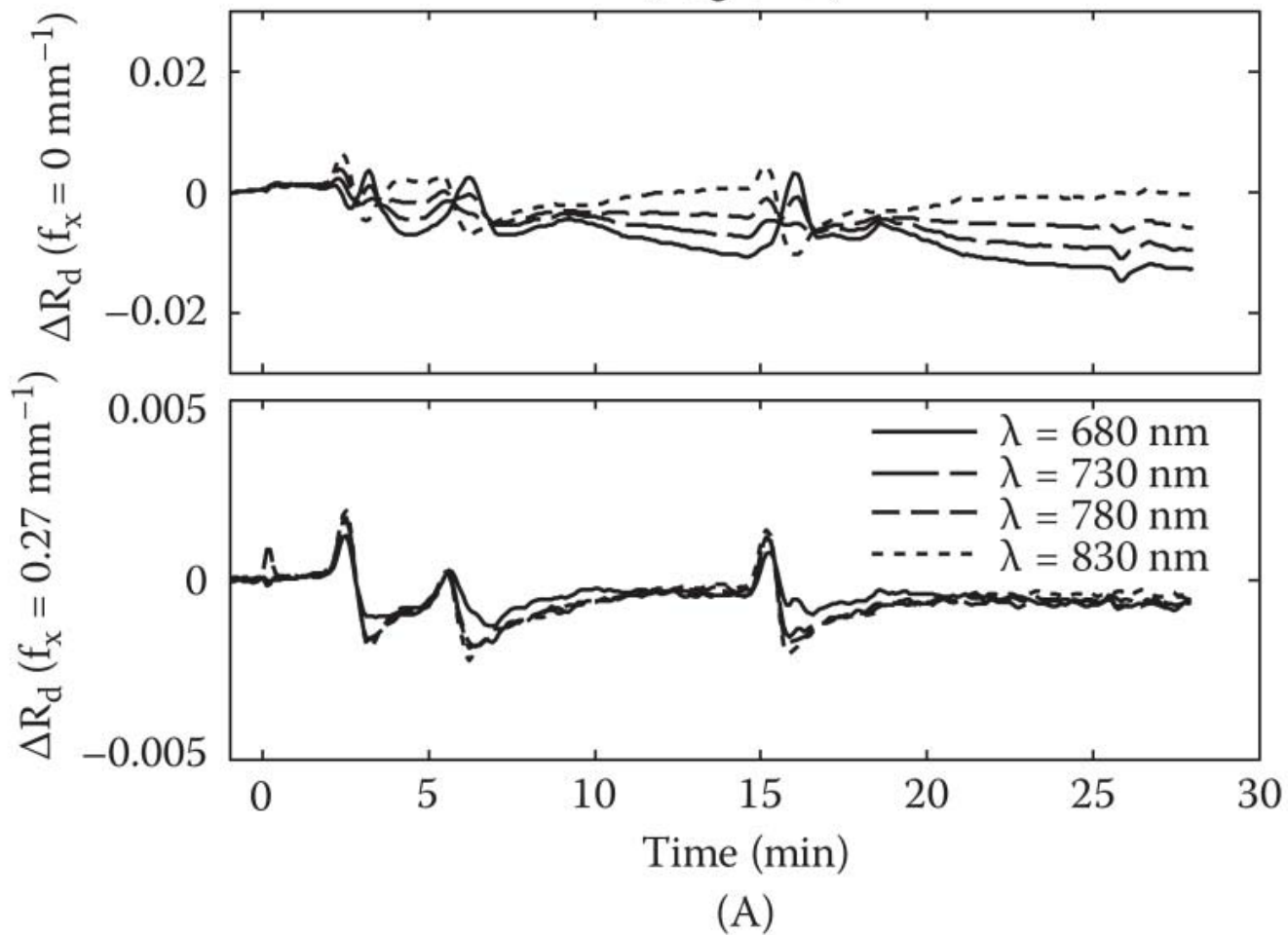
(B)
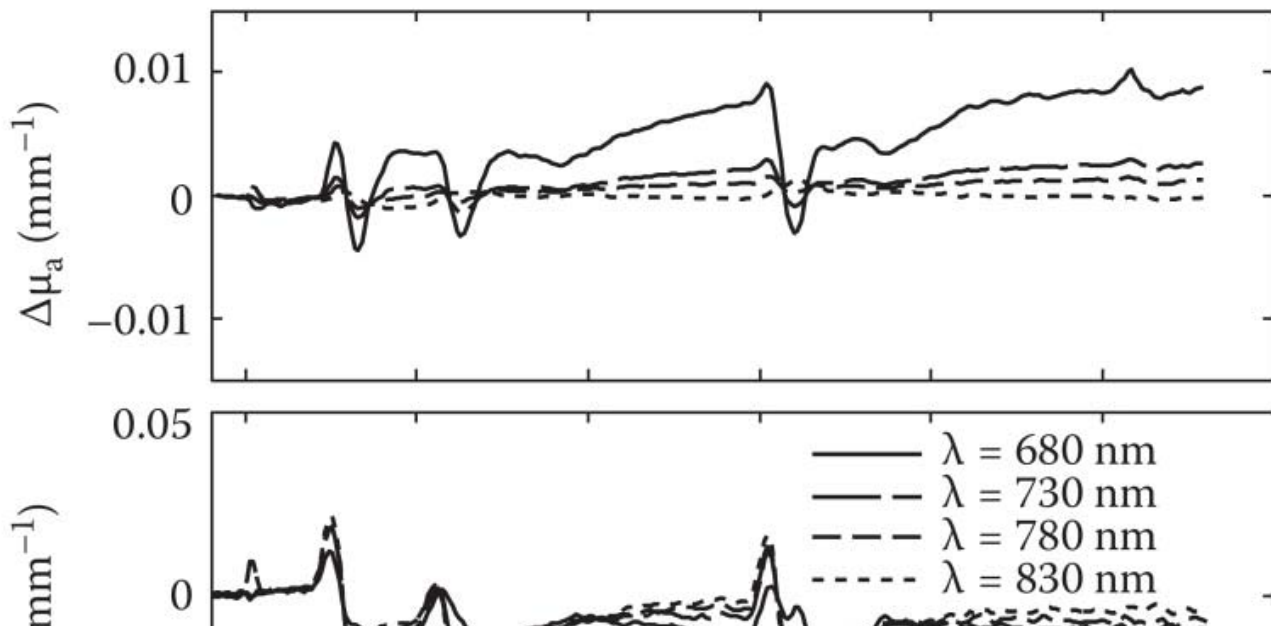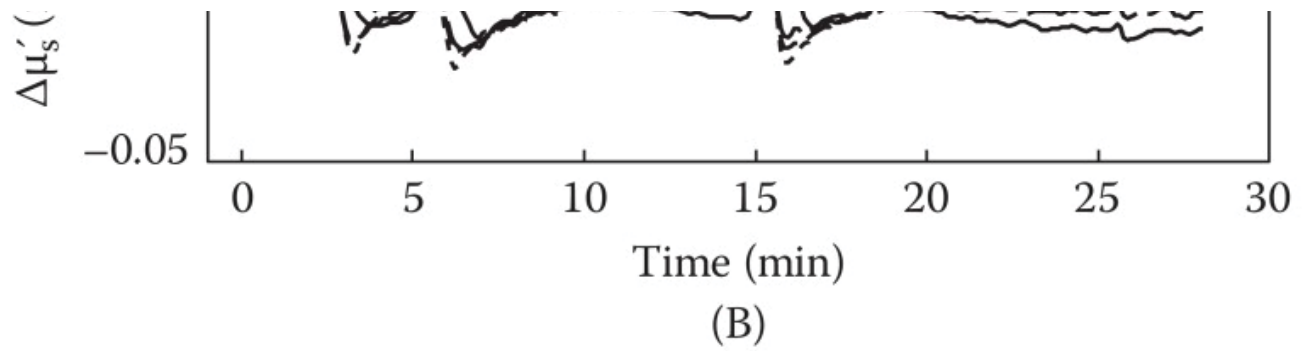
FIGURE 12.8

(A) Multispectral diffuse reflectance at DC ($f_x = 0$ mm^{-1}, top) and DC ($f_x = 0.26$ mm^{-1}, bottom) for Region B of rat 3 over approximately 30 min. (B) Corresponding recovered multispectral absorption (top) and reduced scattering (bottom) coefficients.

Rat 3–CSD: ΔDiffuse Reflectance (R_d) vs. Time (Region C)

$\lambda = 680$ nm
$\lambda = 730$ nm
$\lambda = 780$ nm
$\lambda = 830$ nm

Time (min)

(A)

Rat 3–CSD: ΔOptical Properties (μ_a, μ_s') vs. Time (Region C)

$\lambda = 680$ nm
$\lambda = 730$ nm
$\lambda = 780$ nm
$\lambda = 830$ nm

FIGURE 12.9

(A) Multispectral diffuse reflectance at DC ($fx = 0$ mm^{-1}, top) and DC ($fx = 0.26$ mm^{-1}, bottom) for Region C of rat 3 over approximately 30 min. (B) Corresponding recovered multispectral absorption (top) and reduced scattering (bottom) coefficients.

FIGURE 12.10

Recovered HbR, HbO₂, HbT, and STO2, for ROIs A, B, and C (top, middle, and bottom), recovered by analysis of the multispectral absorption coefficients from Figures 12.7–12.9b (top).

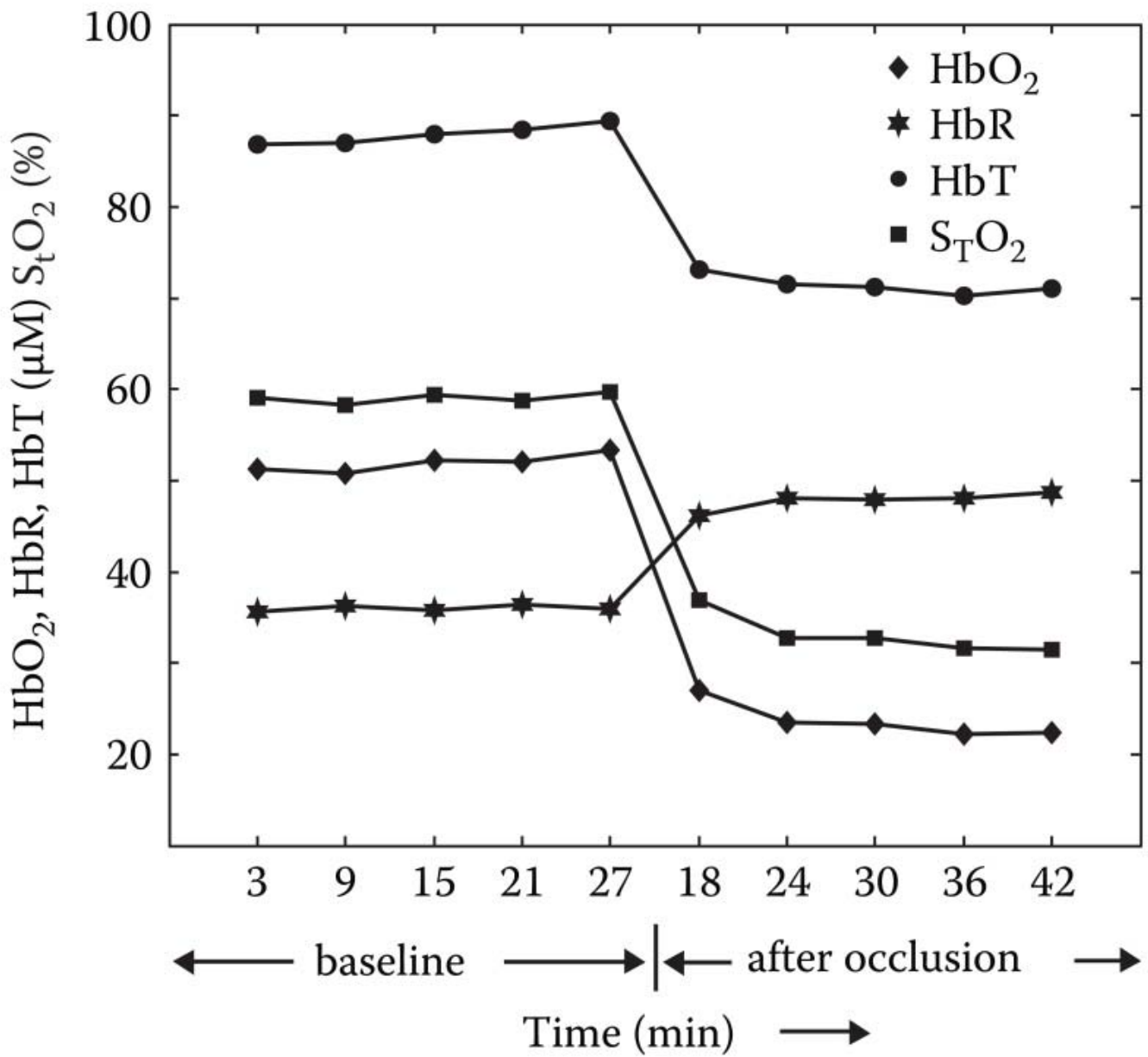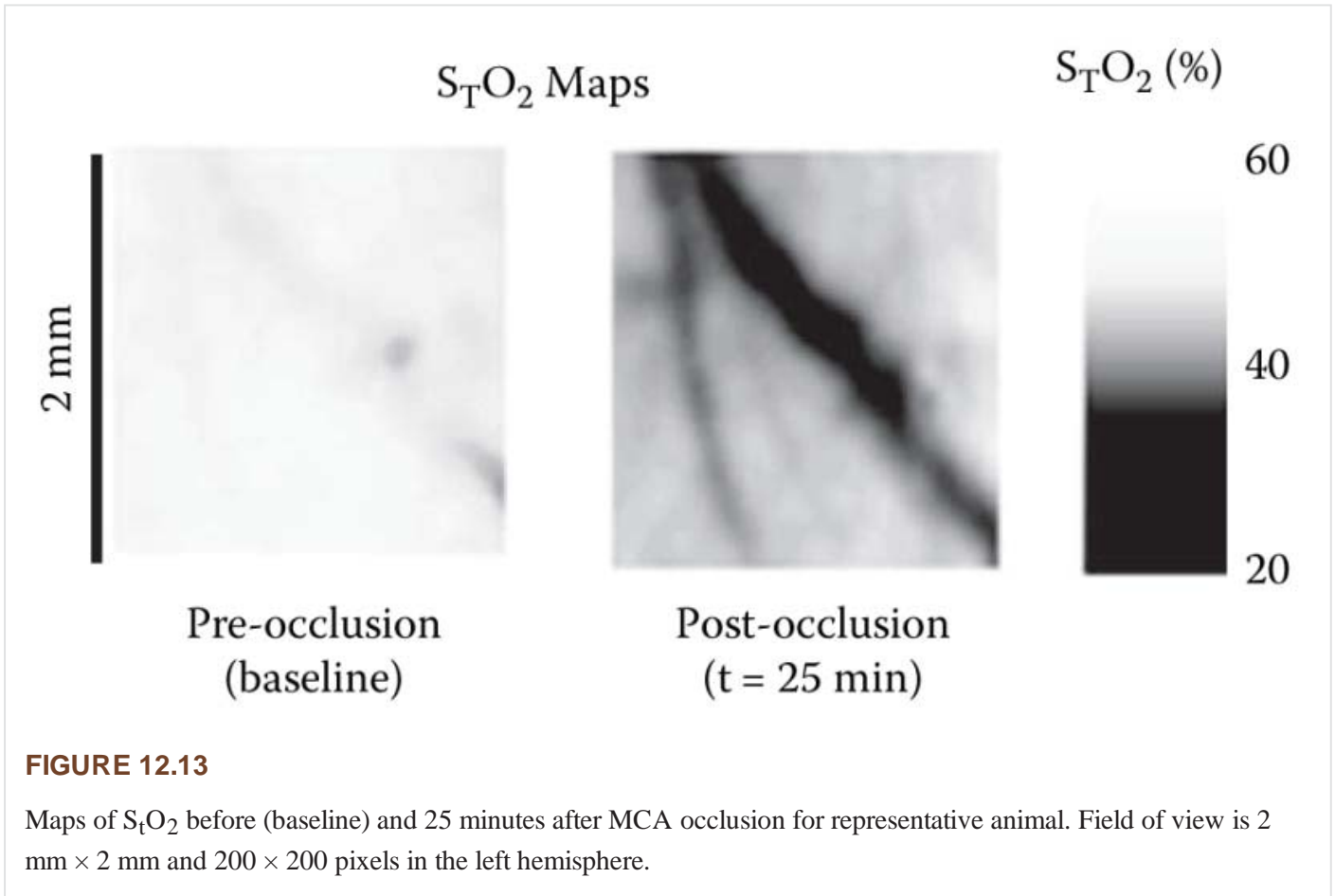| Time (min)	ΔHbO_2 (μm/min)	ΔHbR (μm/min)	ΔHbT (μm/min)	$\Delta S_T O_2$ (%/min)	μ_s', 800 nm (mm^{-1}/min)
1.9					
2.2					
2.5					
2.8					
3.1					
3.4					
3.7					
4.0					
4.3					
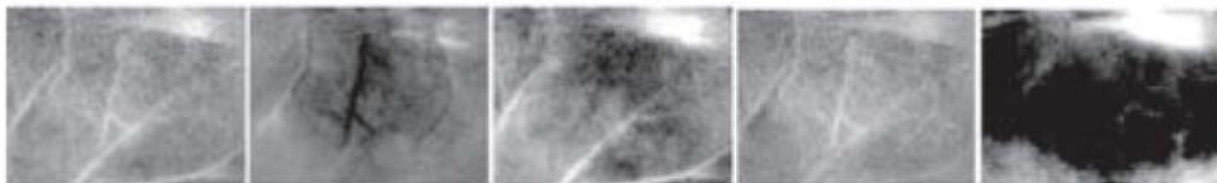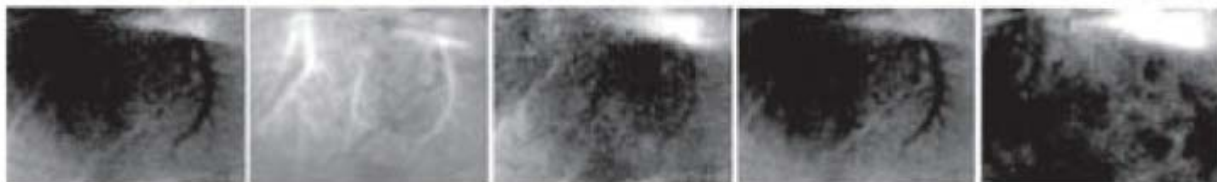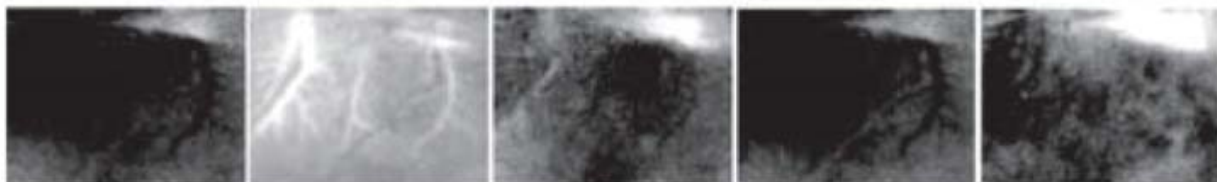
FIGURE 12.12

Mean values of cerebral components before and after MCA occlusion for a single representative animal. Hemoglobin and saturation parameters were calculated from wavelength-dependent optical properties for each pixel (680, 800, 880, 920, and 980 nm), then averaged over the entire field of view (2 mm × 2 mm, 200 × 200 pixels) in the left hemisphere.

FIGURE 12.13

Maps of S_tO_2 before (baseline) and 25 minutes after MCA occlusion for representative animal. Field of view is 2 mm × 2 mm and 200 × 200 pixels in the left hemisphere.